

Dirac and Chiral Quantum Spin Liquids on the Honeycomb Lattice in a Magnetic Field

Zheng-Xin Liu¹ and B. Normand²

¹*Department of Physics, Renmin University of China, Beijing 100872, China*

²*Neutrons and Muons Research Division, Paul Scherrer Institute, CH-5232 Villigen-PSI, Switzerland*

Motivated by recent experimental observations in α -RuCl₃, we study the K - Γ model on the honeycomb lattice in an external magnetic field. By a slave-particle representation and Variational Monte Carlo calculations, we reproduce the phase transition from zigzag magnetic order to a field-induced disordered phase. The nature of this state depends crucially on the field orientation. For particular field directions in the honeycomb plane, we find a gapless Dirac spin liquid, in agreement with recent experiments on α -RuCl₃. For a range of out-of-plane fields, we predict the existence of a Kalmeyer-Laughlin-type chiral spin liquid, which would show an integer-quantized thermal Hall effect.

The Kitaev model on the honeycomb lattice [1] is exactly solvable and thus presents a fundamental paradigm for both gapped and gapless quantum spin liquids (QSLs). An applied magnetic field can turn the gapless phase into a gapped, non-Abelian QSL, which would have direct applications in topological quantum computation [2]. Although Kitaev-type interactions are realized in layered honeycomb-lattice materials, such as Na₂IrO₃ [3–7] and α -RuCl₃ [8–10], their magnetically ordered ground states [6, 7, 11–14], preclude a QSL and indicate significant non-Kitaev interactions [4, 15]. Nevertheless, experimental observations of a continuum by inelastic neutron scattering (INS) [16] and a gapless mode at intermediate fields by thermal conductivity [17] have been taken as evidence for the proximity of α -RuCl₃ to Kitaev physics.

Recent experiments have established that magnetic order in α -RuCl₃ is weak and can be suppressed both by a magnetic field [17–19] and by pressure [20, 21]. The critical field, when applied in the honeycomb (ab) plane, is $B_c = 7.5$ T [17, 19], which is far below the saturation field [22], and the resulting partially polarized but magnetically disordered state has been claimed to be a QSL. Numerous very recent studies of this phase are divided as to its nature, with nuclear magnetic resonance (NMR) in an out-of-plane field [18], specific heat [23, 24], and neutron spectroscopy [25] reporting a gapped QSL, whereas power-law temperature dependences observed by thermal conductivity [17] and NMR in an in-plane field [19] suggest a gapless (nodal) QSL. NMR is a particularly sensitive probe of low-energy spin excitations and the spin-lattice relaxation rate, $1/T_1 \propto T^3$, observed [19] at $T < 10$ K over a finite field range $7.5 \text{ T} < B < 12$ T matches precisely the result anticipated for the point-node dispersion of a generic Kitaev system [26], albeit only at zero field. Because such nodal excitations are neither magnons nor the Majorana fermions of the Kitaev QSL, both of which show a gapped spin response in a field [27], their existence would pose a theoretical challenge. Because their density of states vanishes as energy approaches zero, their detection and distinction from a fully gapped phase poses a subtle experimental challenge.

In this Letter we analyze the low-energy physics of the

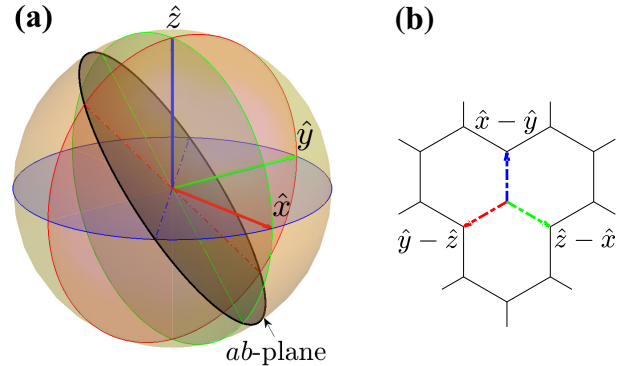


FIG. 1. (a) Field directions in the honeycomb system represented on the surface of a sphere. The dark plane is the lattice ab plane. \hat{x} , \hat{y} , and \hat{z} are the Kitaev axes of spins residing on the three different bonds [panel (b)]. Red, green, and blue planes are those normal to the respective spin axes. (b) Relation between lattice and spin basis vectors.

field-induced magnetically disordered phase in α -RuCl₃. We employ a slave-fermion representation to demonstrate that the properties of this state depend strongly on the direction of the applied field, which can produce a gapless Dirac QSL, a gapped chiral QSL, or a gapped and topologically trivial paramagnetic phase. By Variational Monte Carlo (VMC) calculations using Gutzwiller-projected states, we obtain a semi-quantitative description of the suppression of low-field order and deduce the dispersions and phase diagrams in all three cases.

We begin with a minimal effective model containing only Kitaev (K) and symmetric off-diagonal (Γ) terms,

$$H = \sum_{(i,j) \in \alpha\beta(\gamma)} [K S_i^\gamma S_j^\gamma + \Gamma (S_i^\alpha S_j^\beta + S_i^\beta S_j^\alpha)] + g\mu_B \sum_i \mathbf{B} \cdot \mathbf{S}_i. \quad (1)$$

We neglect Heisenberg exchange terms, which are argued to be small in a perturbative expansion [28]. We adopt the representative parameters $K = -6.8\text{meV}$ and $\Gamma = 9.5\text{meV}$ used to fit the spin-wave spectrum of α -RuCl₃ measured by INS [29], which places the system far from the (generic) Kitaev regime [26]. Within this model we

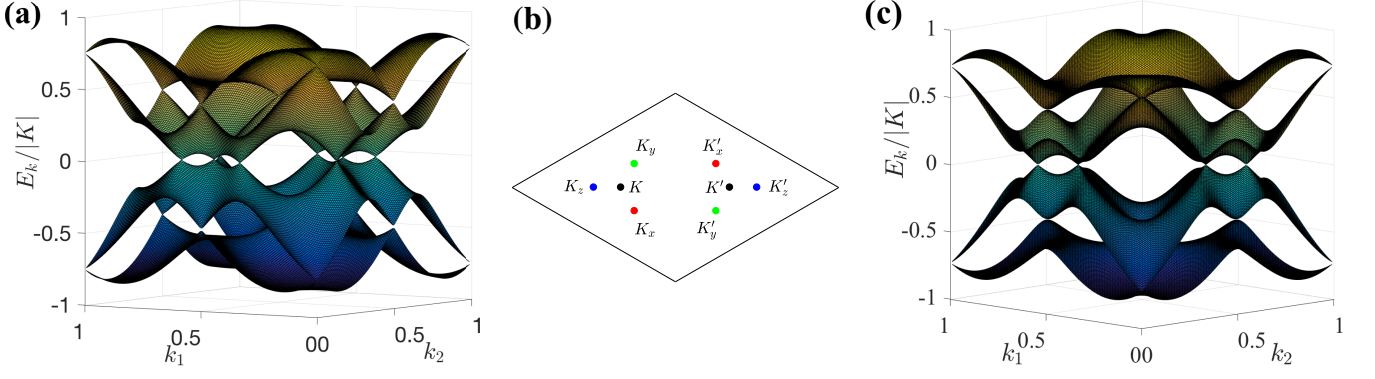


FIG. 2. (a) Spinon dispersion with $\mathbf{B} = 0$, showing eight Dirac cones. (b) Locations of the eight nodes in the Brillouin zone. (c) Spinon dispersion with an in-plane field $\mathbf{B} \parallel (\hat{x} - \hat{y})$, showing two remaining pairs of Dirac cones close to K, K' and K_x, K'_x .

treat the Landé g factor as isotropic ($g = 2$) [30].

Chemical coordination and spin-orbit coupling (SOC) in Na_2IrO_3 and $\alpha\text{-RuCl}_3$ fix the spin axes of the Kitaev interaction terms to the lattice such that the crystalline c axis is the $[111]$ direction in the spin frame, as represented in Fig. 1(a). The lattice bond directions, which lie in the ab plane and will turn out to have particular significance, are $(\hat{x} - \hat{y})$, $(\hat{y} - \hat{z})$, and $(\hat{z} - \hat{x})$ in the spin basis [Fig. 1(b)]. $\alpha\text{-RuCl}_3$ has space-group symmetry P3_112 , whose point group is D_3 . However, we restrict our considerations to a single honeycomb layer, which has point group D_{3d} when the applied field $\mathbf{B} = 0$, and any lattice rotation is associated with a spin rotation due to SOC. A QSL state should break neither translation nor any of the symmetries remaining in the presence of \mathbf{B} .

Our analysis is based on a slave-particle representation in which spin operators at site i are represented by two species of fermionic spinon, taking the quadratic forms $S_i^m = \frac{1}{2} C_i^\dagger \sigma_m C_i$, where $C_i^\dagger = (c_{i\uparrow}^\dagger, c_{i\downarrow}^\dagger)$, $m = x, y, z$, σ_m are the Pauli matrices, and the spinons obey the on-site particle-number constraint $\hat{N}_i = c_{i\uparrow}^\dagger c_{i\uparrow} + c_{i\downarrow}^\dagger c_{i\downarrow} = 1$. By applying the mean-field approximation detailed in Sec. S1 of the Supplemental Material (SM) [33], we express the K - Γ model in the form

$$H_{\text{mf}} = \sum_{\langle ij \rangle \in \alpha\beta(\gamma)} [C_i^\dagger (t_1^\gamma R_{\alpha\beta} - it_0^\gamma + t_2^\gamma \sigma_\gamma) C_j + \text{h.c.}] + g\mu_B \sum_i C_i^\dagger (\frac{1}{2} \mathbf{B} \cdot \boldsymbol{\sigma} + \lambda) C_i + H_0, \quad (2)$$

where $R_{\alpha\beta} = \frac{-i}{\sqrt{2}}(\sigma_\alpha + \sigma_\beta)$, $t_1^\gamma = -\frac{1}{2}|K|\langle C_i^\dagger R_{\alpha\beta} C_j \rangle^*$, $t_{0,2}^\gamma = -\frac{1}{8}(\Gamma - |K|)[\langle C_i^\dagger \sigma_\alpha R_{\alpha\beta} C_j \rangle^* \pm \langle C_i^\dagger \sigma_\beta R_{\alpha\beta} C_j \rangle^*]$, λ , a Lagrange multiplier corresponding to the average particle-number constraint, functions as a chemical potential, and H_0 is a constant. The t_1^γ and t_2^γ terms are analogous to the Rashba SOC of electrons [31]. We will determine all of these parameters by VMC calculations in which the local constraint is enforced exactly.

Before turning to this quantitative treatment, we consider the qualitative nature of the mean-field spinon state and its response to a magnetic field. The mean-field

state is by construction a QSL, which in Eq. (S5) has $U(1)$ gauge symmetry because the spinon number is conserved. Finite spinon pairing terms may result in a Z_2 QSL [32], but are neglected in Eq. (S5) because we have found (Sec. S1 of the SM [33]) that they are not favored energetically at intermediate magnetic fields.

The honeycomb lattice usually supports a conical spectrum due to its C_{3v} point-group symmetry. In graphene the K and K' points are invariant under C_{3v} , whose two-dimensional irreducible representation results in two-fold energetic degeneracies and hence in Dirac cones. These cones can be gapped in two ways, one being to add a sublattice chemical potential, μ_z , which breaks the symmetry down to C_3 . The alternative, which does not break the symmetry explicitly, is that increasing strain causes the two cones to move together adiabatically until they merge into a single branch, whose “semi-Dirac” [44] dispersion is quadratic in one \mathbf{k} -space direction but remains linear in the other, after which a full gap opens.

For illustration, we take $t_1^\gamma = 1$, $t_0^\gamma = t_2^\gamma = 0$ in Eq. (S5). When $\mathbf{B} = 0$, the spinon dispersion [Fig. 2(a)] is gapless with eight Dirac cones in the Brillouin zone [Fig. 2(b)]. These conical dispersions are protected by (emergent) symmetries, which separate them into two types.

(1) At K and K' , C_{3v} is preserved even with SOC and protects the cones. The generators of the C_{3v} group are

$$C_3 = e^{\mp i \frac{2\pi}{3} \frac{\mu_z}{2}} \otimes e^{-i \frac{2\pi}{3} \frac{\sigma_c}{2\sqrt{3}}}, M_z = \mu_\pm \otimes \frac{1}{\sqrt{2}}(\sigma_x - \sigma_y), \quad (3)$$

at K and K' respectively, where μ_m are Pauli matrices operating on the sublattice indices, $\mu_\pm = \pm \frac{1}{2}\mu_x + \frac{\sqrt{3}}{2}\mu_y$, and $\sigma_c = \boldsymbol{\sigma} \cdot \hat{c}$ with $\hat{c} = \frac{1}{\sqrt{3}}(\hat{x} + \hat{y} + \hat{z})$. Like a μ_z term, a field (Zeeman) term, $H' = B_c \sigma_c$, also breaks the mirror symmetry, gapping the cones at K and K' . Unlike μ_z , which creates a trivial gapped phase, B_c gives a nonzero Chern number, as detailed in Sec. S2 of the SM [33].

(2) At the K_x and K'_x points, expansion of Eq. (S5) in momentum space gives an effective Hamiltonian with C_{4v} symmetry, whose generators are represented as

$$C_4 = e^{\mp i \mu_z \frac{\pi}{4}} \otimes e^{i \sigma_x \frac{\pi}{4}}, M_x = \mu_x \otimes \frac{1}{\sqrt{2}}(\sigma_y - \sigma_z), \quad (4)$$

at K_x and K'_x respectively. Because the momentum itself is not invariant under C_{4v} , this is an emergent symmetry, which is interpreted as operations with sublattice-spin coupling but without spatial rotation. As above, a magnetic field along \hat{x} gaps the cones, with the key difference that the mass B_x has the opposite sign to the mass B_c for the cones at K and K' [cf. Eqs. (3) and (4)], which has important consequences for the total Chern number. The same physics applies to the Dirac cones at K_y, K'_y and K_z, K'_z in fields B_y and B_z .

These results are summarized in Table I, where we have assumed that the Dirac cones are independent. Clearly if the magnetic field is oriented such that $\mathbf{B} \perp \hat{\alpha}$ and $\mathbf{B} \perp \hat{\beta}$ ($\alpha, \beta = c, x, y, z$), i.e. at any intersection of the circles on the sphere in Fig. 1(a), then two pairs of Dirac cones have vanishing masses, as shown in Fig. 2(c). These cones are symmetry-protected and cannot be gapped individually. With increasing field, the cones of each pair move together, merging to a semi-Dirac dispersion, and then open a full gap, as shown in Sec. S3 of the SM [33].

For fields $\mathbf{B} \perp \hat{\alpha}$, i.e. any other points on the circles in Fig. 1(a), one pair of Dirac cones retains a vanishing linear mass and one may expect the spinons to remain gapless. However, higher-order processes generate a small gap that scales algebraically with the field, $\Delta = c|\mathbf{B}|^a$. We present some numerical results for a in Sec. S3 of the SM [33]; as an example, $a = 2.4$ if $\mathbf{B} \parallel (\hat{x} + \hat{y})$. The resulting slow growth of this gap may cause it to remain below the measurement temperature over a broad field range, making the system behave as if it were still gapless. This explains qualitatively the appearance of point-node excitations for all in-plane field directions in NMR [19].

For all other field directions, all the cones have nonzero masses and the spinon dispersion has a gap, which opens linearly in $|\mathbf{B}|$. The total Chern number of the half-filled fully gapped bands is $\mathcal{C} = \text{sgn}(\mathbf{B} \cdot \hat{x}) + \text{sgn}(\mathbf{B} \cdot \hat{y}) + \text{sgn}(\mathbf{B} \cdot \hat{z}) - \text{sgn}(\mathbf{B} \cdot \hat{c})$, which is either 0 or ± 2 . If a point on the sphere of Fig. 1(a) is surrounded by only three arcs, then $\mathcal{C} = \pm 2$ and a chiral QSL is obtained, which persists up to a critical value of $|\mathbf{B}|$ where its gap closes (Sec. S3 of the SM [33]). If a point is surrounded by four arcs, then $\mathcal{C} = 0$ and the gap never closes at finite $|\mathbf{B}|$, meaning that the system is connected adiabatically to the fully polarized trivial (direct-product) state.

The topological transition between the $\mathcal{C} = 0$ and ± 2 regimes is a function of field angle and is discussed in Sec. S4 of the SM [33]. We recall that the field-induced QSL states we find have U(1) gauge symmetry, in contrast to the Z_2 gauge symmetry and finite vison gap of

Dirac node	Mass	Sign of mass	Chern number
K, K'	$\mathbf{B} \cdot \hat{c}$	-	$-\text{sgn}(\mathbf{B} \cdot \hat{c})$
K_x, K'_x	$\mathbf{B} \cdot \hat{x}$	+	$\text{sgn}(\mathbf{B} \cdot \hat{x})$
K_y, K'_y	$\mathbf{B} \cdot \hat{y}$	+	$\text{sgn}(\mathbf{B} \cdot \hat{y})$
K_z, K'_z	$\mathbf{B} \cdot \hat{z}$	+	$\text{sgn}(\mathbf{B} \cdot \hat{z})$

TABLE I. Action of magnetic fields in giving mass to the Dirac cones of Fig. 2(a).

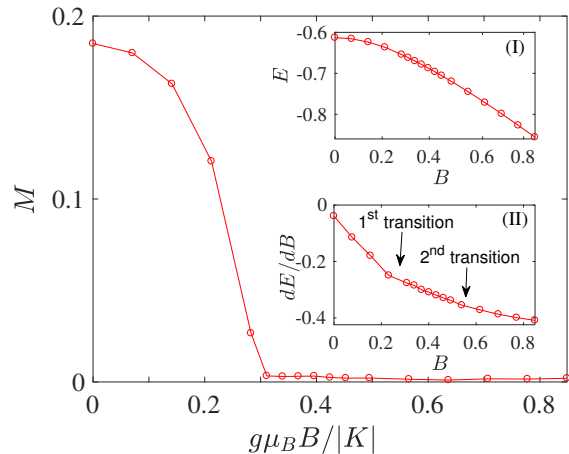


FIG. 3. Magnetization as a function of field for $\mathbf{B} \parallel (\hat{x} - \hat{y})$. Inset (I) shows the ground-state energy, E , as a function of B . Inset (II) shows dE/dB , whose discontinuity coincides with the magnetic transition. At the weak second transition, the Dirac cones become gapped.

the Kitaev QSLs. In two spatial dimensions, U(1) gauge fields are confined, which is the trivial gapped phase, unless the matter (spinon) field is gapless, which is our four-cone case, or there is a Chern-Simons term, which is our $\mathcal{C} = \pm 2$ case. The transition may therefore be considered as a spinon (de)confinement process and its position obtained from the spinon dispersion and Chern number.

Thus at the mean-field level we have obtained crucial qualitative insight into the physical properties of three different field-induced disordered phases. However, the ground state observed in α -RuCl₃ is a zigzag magnetic order [11–14], which some authors [15] find in the classical K - Γ model (1), whereas others [30] find that a small ferromagnetic (FM) Heisenberg interaction is required to stabilize it. In Sec. S1 of the SM [33] we discuss the quantum model and show that our results are reinforced by FM terms. To compare with experimental data, we introduce zigzag order within the single- Q approximation, $\mathbf{M}_i = M(\sin \eta [\hat{e}_i^x \cos(\mathbf{Q} \cdot \mathbf{r}_i) + \hat{e}_i^y \sin(\mathbf{Q} \cdot \mathbf{r}_i)] + \cos \eta \hat{e}_i^z)$, where $\mathbf{Q} = [1/2, 1/2]$, the local (spin) axes, \hat{e}_i^α , are fixed by the classical ground state, and η is the canting angle. We treat the static order as an external field to obtain a new mean-field Hamiltonian, $H'_{\text{mf}} = H_{\text{mf}} - \sum_i (\frac{1}{2} \mathbf{M}_i \cdot \mathbf{C}_i^\dagger \boldsymbol{\sigma} \mathbf{C}_i + \text{h.c.})$; in a variational treatment, this process is equivalent to introducing an additional decoupling channel in H_{mf} (Sec. S1 of the SM [33]).

VMC calculations are based on the mean-field states but enforce the local constraint on spinon number by Gutzwiller projection. This method has been applied widely to capture the essential physics of correlated electron systems and in certain cases, including slave-parton approaches to QSL states, can provide exact information. Here we employ the variational wave functions $|\psi_G(\mathbf{p})\rangle = P_G |\psi_{\text{mf}}(\mathbf{p})\rangle$, where \mathbf{p} denotes $(t_0^\gamma, t_1^\gamma, t_2^\gamma, \lambda, M, \eta)$, to obtain the optimal state by minimizing the ground-state

energy, $E = \frac{\langle \psi_G | H | \psi_G \rangle}{\langle \psi_G | \psi_G \rangle}$, on a system of 128 sites and use it to compute physical expectation values. To benchmark the accuracy of our results, in a small (8-site) system we obtain an overlap $\langle \psi_{\text{VMC}} | \psi_{\text{ED}} \rangle = 0.988$ between the VMC and exact-diagonalization wave functions (more details are provided in Sec. S1 of the SM [33]).

We establish magnetic phase diagrams by fixing the field direction and increasing its magnitude. Zigzag order is suppressed for all field directions and vanishes at a lower critical field (Fig. 3), beyond which, as anticipated from the mean-field analysis, three different field-induced (partially polarized) disordered phases appear.

Dirac QSL. If $\mathbf{B} \parallel \hat{\alpha}$ or $\mathbf{B} \parallel (\hat{\alpha} - \hat{\beta})$ ($\alpha, \beta = x, y, z$), there are two critical points, as shown in Fig. 4(a). The first marks the continuous transition from the ordered phase to a disordered one (Fig. 3) in which the spinon dispersion, with optimized parameters determined from VMC, is gapless. Thus the intermediate phase is a stable U(1) Dirac QSL. At the second transition, which is also continuous, a gap opens as the system enters the trivial paramagnetic phase.

Chiral QSL. If $\mathcal{C} = \pm 2$, for example when $\mathbf{B} \parallel \hat{c}$ or $\mathbf{B} \parallel (\hat{x} + \hat{y} + \frac{1}{2}\hat{z})$ [Fig. 4(b)], the disordered phase is a chiral QSL [47, 48]. This state is gapped, Abelian, has chiral edge modes, supports semionic spinon excitations, and has an integer-quantized thermal Hall conductivity, which can be measured in experiment. It exists over a continuous regime of applied field directions, upon which the critical field depends strongly (numerically determined values include $g\mu_B B/|K| \simeq 2.4$ for $\mathbf{B} \parallel \hat{c}$ and 0.3 for $\mathbf{B} \parallel (\hat{x} + \hat{y} + \frac{1}{2}\hat{z})$ [Fig. 4(b)]). At a higher critical point, the chiral QSL undergoes a transition to the trivial phase.

Gapped paramagnet. For field orientations giving $\mathcal{C} = 0$, and for the cases where the field direction lies on the circles in Fig. 1(a), the phase diagram has only one critical point [Fig. 4(c)]. This separates the ordered phase from the trivial polarized phase, whose gap opens linearly with field, except on the special lines where it opens algebraically with a higher power.

We have analyzed the spin-liquid state within a slave-particle representation, which is uncontrolled. However, VMC studies allowing accurate enforcement of the constraint reveal only moderate quantitative alterations to the results. This indicates that the spinon description is well able to capture all the significant magnetic degrees of freedom. We stress that the gapless spin excitations of the field-induced U(1) QSL are deconfined Dirac fermions, which are different from the Majorana fermions in the gapless Kitaev QSL. Indeed, our results show that Kitaev QSLs are poor trial states, giving much higher energies than the U(1) QSL for the model of Eq. (1) with $\Gamma/|K| = 1.4$. To address the stability of the U(1) QSL, we have tested the possibility of spinon pairing, but show in Sec. S1 of the SM [33] that this is not favorable. However, here we do not try to classify and test all possible

QSL states of the model. We comment that recent numerical studies of the K - Γ model [45, 46] also find QSL

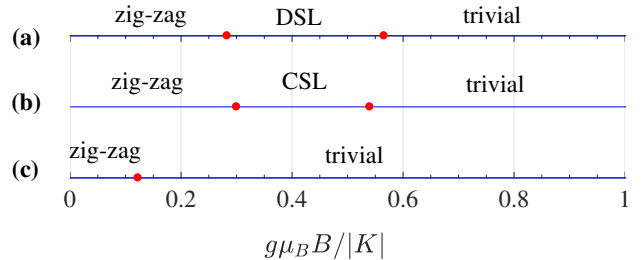


FIG. 4. Phase diagrams for different orientations of \mathbf{B} . (a) $\mathbf{B} \parallel (\hat{x} - \hat{y})$, where the intermediate phase is a field-induced Dirac spin liquid (DSL). Both transitions are of second order. (b) $\mathbf{B} \parallel (\hat{x} + \hat{y} + \frac{1}{2}\hat{z})$, where the intermediate phase is a field-induced chiral spin liquid (CSL). The lower transition is of first order, while the upper is second-order. (c) $\mathbf{B} \parallel (\hat{x} + \hat{y} - 2\hat{z})$, where there is only one, weakly first-order, transition.

states over much of the phase diagram, albeit without detailed consideration of magnetic order or applied fields.

Our conclusions are in quantitative agreement with experiments on α - RuCl_3 . The lower critical fields for the loss of zigzag order fall around 7.5 T for in-plane (ab) fields. Our VMC phase diagrams in this case show that the field-induced disordered phase is either truly gapless for discrete field directions or otherwise has a very small gap that grows algebraically with $|\mathbf{B}|$, such that for temperatures $T \geq 1.5$ K it would appear gapless. These results are fully consistent with recent NMR observations of a spin-lattice relaxation rate $1/T_1 \propto T^3$ and a largely isotropic response for all in-plane field orientations.

In summary, we have studied the K - Γ model on the honeycomb lattice with an external magnetic field. By using Gutzwiller-projected states as variational wave functions and including zigzag magnetic order, we find three different field-induced disordered phases, whose nature varies strongly with the field direction. In certain cases, the intermediate QSL is gapless with Dirac-cone excitations, which are protected by emergent symmetries. In others it is a gapped chiral QSL, which may be sought in experiment through its integer-quantized thermal Hall effect.

Acknowledgments. We are grateful to W. Yu and J. Wen for the experimental collaboration which initiated this study. We thank W. Ku, J.-X. Li, H.-J. Liao, C. Morais Smith, R. Valentí, M. Vojta, F. Wang, X.-Q. Wang, F. Wilczek, T. Xiang, J.-Z. Zhao, and Y. Zhou for helpful discussions. This work was supported by the NSF of China (Grant No. 11574392), the Ministry of Science and Technology of China (Grant No. 2016YFA0300504), and the Fundamental Research Funds for the Central Universities and the Research Funds of Renmin University of China (No. 15XNLF19).

- [1] A. Kitaev, *Ann. Phys.* **321**, 2 (2006).
- [2] C. Nayak, S. H. Simon, A. Stern, M. Freedman, and S. Das Sarma, *Rev. Mod. Phys.* **80**, 1083 (2008).
- [3] G. Jackeli and G. Khaliullin, *Phys. Rev. Lett.* **102**, 017205 (2009).
- [4] J. Chaloupka, G. Jackeli, and G. Khaliullin, *Phys. Rev. Lett.* **105**, 027204 (2010).
- [5] X. Liu, T. Berlijn, W.-G. Yin, W. Ku, A. Tsvelik, Y.-J. Kim, H. Gretarsson, Y. Singh, P. Gegenwart, and J. P. Hill, *Phys. Rev. B* **83**, 220403 (2011).
- [6] F. Ye, S. Chi, H. Cao, B. Chakoumakos, J. A. Fernandez-Baca, R. Custelcean, T. F. Qi, O. B. Korneta, and G. Cao, *Phys. Rev. B* **85**, 180403 (2012).
- [7] S. K. Choi, R. Coldea, A. N. Kolmogorov, T. Lancaster, I. I. Mazin, S. J. Blundell, P. G. Radaelli, Y. Singh, P. Gegenwart, K. R. Choi, S.-W. Cheong, P. J. Baker, C. Stock, and J. Taylor, *Phys. Rev. Lett.* **108**, 127204 (2012).
- [8] I. Pollini, *Phys. Rev. B* **53**, 12769 (1996).
- [9] K. W. Plumb, J. P. Clancy, L. J. Sandilands, V. V. Shankar, Y. F. Hu, K. S. Burch, H.-Y. Kee, and Y.-J. Kim, *Phys. Rev. B* **90**, 041112 (2014).
- [10] H.-S. Kim, V. V. Shankar, A. Catuneanu, and H.-Y. Kee, *Phys. Rev. B* **91**, 241110 (2015).
- [11] J. M. Fletcher, W. E. Gardner, A. C. Fox, and G. Topping, *J. Chem. Soc. A* 1038 (1967).
- [12] J. A. Sears, M. Songvilay, K. W. Plumb, J. P. Clancy, Y. Qiu, Y. Zhao, D. Parshall, and Y.-J. Kim, *Phys. Rev. B* **91**, 144420 (2015).
- [13] R. D. Johnson, S. C. Williams, A. A. Haghighirad, J. Singleton, V. Zapf, P. Manuel, I. I. Mazin, Y. Li, H. O. Jeschke, R. Valentí, and R. Coldea, *Phys. Rev. B* **92**, 235119 (2015).
- [14] H. B. Cao, A. Banerjee, J.-Q. Yan, C. A. Bridges, M. D. Lumsden, D. Mandrus, D. A. Tennant, B. Chakoumakos, and S. E. Nagler, *Phys. Rev. B* **93**, 134423 (2016).
- [15] J. G. Rau, E. K.-H. Lee, and H.-Y. Kee, *Phys. Rev. Lett.* **112**, 077204 (2014).
- [16] A. Banerjee, C. A. Bridges, J. Q. Yan, A. A. Aczel, L. Li, M. B. Stone, G. E. Granroth, M. D. Lumsden, Y. Yiu, J. Knolle, S. Bhattacharjee, D. L. Kovrizhin, R. Moessner, D. A. Tennant, D. G. Mandrus, and S. E. Nagler, *Nat Mater* **15**, 733 (2016).
- [17] I. A. Leahy, C. A. Pocs, P. E. Siegfried, D. Graf, S.-H. Do, K.-Y. Choi, B. Normand, and M. Lee, *Phys. Rev. Lett.* **118**, 187203 (2017).
- [18] S.-H. Baek, S.-H. Do, K.-Y. Choi, Y. S. Kwon, A. U. B. Wolter, S. Nishimoto, J. van den Brink, and B. Büchner, *Phys. Rev. Lett.* **119**, 037201 (2017).
- [19] J. Zheng, K. Ran, T. Li, J. Wang, P. Wang, B. Liu, Z.-X. Liu, B. Normand, J. Wen, and W. Yu, *Phys. Rev. Lett.* **119**, 227208 (2017).
- [20] Z. Wang, J. Guo, F. F. Tafti, A. Hegg, S. Sen, V. A. Sidorov, L. Wang, S. Cai, W. Yi, Y. Zhou, H. Wang, S. Zhang, K. Yang, A. Li, X. Li, Y. Li, J. Liu, Y. Shi, W. Ku, Q. Wu, R. J. Cava, and L. Sun, *unpublished* (arXiv:1705.06139).
- [21] Y. Cui, J. Zheng, K. Ran, J. Wen, Z.-X. Liu, B. Liu, W. Guo, and W. Yu, *Phys. Rev. B* **96**, 205147 (2017).
- [22] R. D. Johnson, S. C. Williams, A. A. Haghighirad, J. Singleton, V. Zapf, P. Manuel, I. I. Mazin, Y. Li, H. O. Jeschke, R. Valentí, and R. Coldea, *Phys. Rev. B* **92**, 235119 (2015).
- [23] J. A. Sears, Y. Zhao, Z. Xu, J. W. Lynn, and Y.-J. Kim, *Phys. Rev. B* **95**, 180411 (2017).
- [24] A. U. B. Wolter, L. T. Corredor, L. Janssen, K. Nenkov, S. Schönecker, S.-H. Do, K.-Y. Choi, R. Albrecht, J. Hunger, T. Doert, M. Vojta, and B. Büchner, *Phys. Rev. B* **96**, 041405 (2017).
- [25] A. Banerjee, P. Lampen-Kelley, J. Knolle, C. Balz, A. A. Aczel, B. Winn, Y. Liu, D. Pajerowski, J.-Q. Yan, C. A. Bridges, A. T. Savici, B. C. Chakoumakos, M. D. Lumsden, D. A. Tennant, R. Moessner, D. G. Mandrus, and S. E. Nagler, *Quantum Materials* **3**, 8 (2018).
- [26] X.-Y. Song, Y.-Z. You, and L. Balents, *Phys. Rev. Lett.* **117**, 037209 (2016).
- [27] J. Knolle, D. L. Kovrizhin, J. T. Chalker, and R. Moessner, *Phys. Rev. Lett.* **112**, 207203 (2014).
- [28] W. Wang, Z.-Y. Dong, S.-L. Yu, and J.-X. Li, *Phys. Rev. B* **96**, 115103 (2017).
- [29] K. Ran, J. Wang, W. Wang, Z.-Y. Dong, X. Ren, S. Bao, S. Li, Z. Ma, Y. Gan, Y. Zhang, J. T. Park, G. Deng, S. Danilkin, S.-L. Yu, J.-X. Li, and J. Wen, *Phys. Rev. Lett.* **118**, 107203 (2017).
- [30] L. Janssen, E. C. Andrade, and M. Vojta, *Phys. Rev. B* **96**, 064430 (2017).
- [31] R. van Gelderen and C. M. Smith, *Phys. Rev. B* **81**, 125435 (2010).
- [32] Y.-Z. You, I. Kimchi, and A. Vishwanath, *Phys. Rev. B* **86**, 085145 (2012).
- [33] For details see the supplemental material at [url], which contains Refs. [34–43].
- [34] I. Affleck, Z. Zou, T. Hsu, and P. W. Anderson, *Phys. Rev. B* **38**, 745 (1988).
- [35] N. Nagaosa, *Quantum Field Theory in Strongly Correlated Electronic Systems*, (Springer, Heidelberg, 1999).
- [36] X.-G. Wen, *Phys. Rev. B* **65**, 165113 (2002).
- [37] Z.-X. Liu, Y. Zhou, H.-H. Tu, X.-G. Wen, and T.-K. Ng, *Phys. Rev. B* **85**, 195144 (2012).
- [38] S. M. Winter, Y. Li, H. O. Jeschke, and R. Valentí, *Phys. Rev. B* **93**, 214431 (2016).
- [39] S. M. Winter, K. Riedl, D. Kaib, R. Coldea, and R. Valentí, *Phys. Rev. Lett.* **120**, 077203 (2018).
- [40] R. Jackiw, *Phys. Rev. D* **29**, 2375 (1984).
- [41] F. D. M. Haldane, *Phys. Rev. Lett.* **61**, 2015 (1988).
- [42] H. Watanabe, Y. Hatsugai, and H. Aoki, *Phys. Rev. B* **82**, 241403(R) (2010).
- [43] M. Mohr, K. Papagelis, J. Maultzsch, and C. Thomsen, *Phys. Rev. B* **80**, 205410 (2009).
- [44] V. Pardo and W. E. Pickett, *Phys. Rev. Lett.* **102**, 166803 (2009).
- [45] A. Catuneanu, Y. Yamaji, G. Wachtel, H.-Y. Kee, and Y. B. Kim, unpublished (arXiv:1701.07837).
- [46] M. Gohlke, G. Wachtel, Y. Yamaji, F. Pollmann, and Y. B. Kim, *Phys. Rev. B* **97**, 075126 (2018).
- [47] V. Kalmeyer and R. B. Laughlin, *Phys. Rev. Lett.* **59**, 2095 (1987).
- [48] X. G. Wen, F. Wilczek, and A. Zee, *Phys. Rev. B* **39**, 11413 (1989).

Supplemental Material for “Dirac and chiral quantum spin liquids on the honeycomb lattice in a magnetic field”

Zheng-Xin Liu and B. Normand

S1. SLAVE-PARTICLE APPROACH FOR THE QUANTUM SPIN LIQUID

A. Fermionic representation of the K - Γ interaction

In the slave-particle representation employed here, the spin operators at every site i are represented by two fermions, $c_{i\uparrow}^\dagger$ and $c_{i\downarrow}^\dagger$. Because we are concerned only with the spin degrees of freedom, we use the terms “slave fermion” and “spinon” interchangeably. As stated in the main text, the spin operators are expressed as

$$S_i^m = \frac{1}{2} C_i^\dagger \sigma_m C_i, \quad m = x, y, z, \quad (\text{S1})$$

where $C_i^\dagger = (c_{i\uparrow}^\dagger, c_{i\downarrow}^\dagger)$ and σ_m are the Pauli matrices. The space of physical spin states is spanned by the sector with only one spinon per site, giving a local constraint on the net particle number, $\hat{N}_i = c_{i\uparrow}^\dagger c_{i\uparrow} + c_{i\downarrow}^\dagger c_{i\downarrow} = 1$. It has been shown that this representation has an SU(2) gauge symmetry [34]. In terms of these fermionic operators, the conventional two-spin interactions are given up to some unimportant constants by

$$\mathbf{S}_i \cdot \mathbf{S}_j = -\frac{1}{4} (C_i^\dagger C_j C_j^\dagger C_i + C_i^\dagger \bar{C}_j \bar{C}_j^\dagger C_i) \quad (\text{S2})$$

for the antiferromagnetic Heisenberg exchange interaction, where $\bar{C}^\dagger = (-c_\downarrow, c_\uparrow)$, and

$$S_i^m S_j^m = -\frac{1}{8} (C_i^\dagger C_j C_j^\dagger C_i + C_i^\dagger \bar{C}_j \bar{C}_j^\dagger C_i + C_i^\dagger \sigma_m C_j C_j^\dagger \sigma_m C_i + C_i^\dagger \sigma_m \bar{C}_j \bar{C}_j^\dagger \sigma_m C_i) \quad (\text{S3})$$

for the Ising interaction.

To express the K - Γ interactions in fermionic operators, it is advantageous to perform a local basis rotation on one site (j) of each bond. For the example of the z -bond, the spin axes are rotated by π around the direction $\hat{x} + \hat{y}$, giving

$$S_j^{m'} = \frac{1}{2} C_j'^\dagger \sigma_m C_j'$$

with $C_j' = R_{xy} C_j$ and $\bar{C}_j' = R_{xy} \bar{C}_j$, where

$$R_{xy} = e^{-i\frac{\pi}{2\sqrt{2}}(\sigma_x + \sigma_y)} = -\frac{i}{\sqrt{2}}(\sigma_x + \sigma_y).$$

The result is a transformation of the spin operators to

$$S_j^z = -S_j^{z'}, \quad S_j^x = S_j^{y'}, \quad S_j^y = S_j^{x'}.$$

Now the z -bond interaction term,

$$K S_i^z S_j^z + \Gamma (S_i^x S_j^y + S_i^y S_j^x), \quad (\text{S4})$$

takes the form of an XXZ interaction of the new spin operators,

$$\begin{aligned} & |K| S_i^z S_j^{z'} + \Gamma (S_i^x S_j^{x'} + S_i^y S_j^{y'}) \\ & = |K| \mathbf{S}_i \cdot \mathbf{S}'_j + (\Gamma - |K|) [S_i^x S_j^{x'} + S_i^y S_j^{y'}], \end{aligned}$$

which in fermionic form is

$$\begin{aligned} & -\frac{1}{4} \Gamma (C_i^\dagger C_j' C_j'^\dagger C_i + C_i^\dagger \bar{C}_j' \bar{C}_j'^\dagger C_i) \\ & -\frac{1}{8} (\Gamma - |K|) [C_i^\dagger \sigma_x C_j' C_j'^\dagger \sigma_x C_i + C_i^\dagger \sigma_x \bar{C}_j' \bar{C}_j'^\dagger \sigma_x C_i \\ & + C_i^\dagger \sigma_y C_j' C_j'^\dagger \sigma_y C_i + C_i^\dagger \sigma_y \bar{C}_j' \bar{C}_j'^\dagger \sigma_y C_i]. \end{aligned}$$

This procedure is repeated for the interactions on the x - and y -bonds.

B. Mean-field decoupling and spin-liquid symmetry

By gathering all terms and applying the mean-field approximation $-O^\dagger O \approx -\langle O^\dagger \rangle O - \langle O \rangle O^\dagger + \langle O^\dagger \rangle \langle O \rangle$, where our choice of sign specifies attractive interaction terms [35], we decouple the Hamiltonian to obtain a quadratic description of the quantum spin-liquid (QSL) state. In the complete fermionic representation of the K - Γ Hamiltonian, both spinon hopping and spinon pairing terms should have finite expectation values and the full mean-field Hamiltonian is

$$\begin{aligned} H_{\text{mf}} = & \sum_{\langle ij \rangle \in \alpha\beta(\gamma)} \{ [C_i^\dagger (t_1^\gamma R_{\alpha\beta} - it_0^\gamma + t_2^\gamma \sigma_\gamma + t_3^\gamma \sigma_\gamma R_{\alpha\beta}) C_j \\ & + C_i^\dagger (\Delta_1^\gamma R_{\alpha\beta} - i\Delta_0^\gamma + \Delta_2^\gamma \sigma_\gamma + \Delta_3^\gamma \sigma_\gamma R_{\alpha\beta}) \bar{C}_j] + \text{h.c.} \} \\ & + \sum_i C_i^\dagger [\frac{1}{2} (g\mu_B \mathbf{B} - \mathbf{M}_i) \cdot \boldsymbol{\sigma} + \lambda_i] C_i + H_0, \quad (\text{S5}) \end{aligned}$$

where H_0 is an irrelevant constant. \mathbf{M}_i allows magnetic decouplings of the spinon Hamiltonian and is set to zero in Eq. (2) of the main text for the purposes of analyzing the unrestricted mean-field solutions; its role is restored on P3 of the main text for the VMC analysis. λ_i is a Lagrange multiplier for the particle-number constraint on each site, but by translational invariance all λ_i have the same value, λ , which functions as the chemical potential (ensuring that the system remains half-filled with spinons for any value of \mathbf{B}). The mean-field spinon-pairing parameters, $\Delta_{0,1,2,3}^\gamma$, are off-diagonal analogs of the spinon-hopping parameters, $t_{0,1,2}^\gamma$, which are defined below Eq. (2) of the main text, and $t_3^\gamma = -\frac{1}{8} (|K| - \Gamma) \langle C_i^\dagger \sigma_\gamma R_{\alpha\beta} C_j \rangle^*$. While the parameters t_1^γ and Δ_1^γ are finite for all finite $|K|$, $t_{0,2}^\gamma$ and $\Delta_{0,2}^\gamma$ are finite when $\Gamma > |K|$ and t_3^γ and Δ_3^γ when $\Gamma < |K|$. Hence we ignore the last pair of parameters in the present study.

In the absence of spinon pairing ($\Delta_{0,1,2}^\gamma = 0$), spinon number is conserved and the mean-field Hamiltonian (S5) has a U(1) gauge symmetry, which is known as the invariant gauge group [36]. If both the hopping and pairing parameters are nonzero, then the invariant gauge group is generally reduced to Z_2 . The constants $t_{0,1,2}^\gamma$ and $\Delta_{0,1,2}^\gamma$ are treated as variational parameters, which are determined by minimizing the ground-state energy, either at the mean-field level, where the spinon-number constraint is enforced only globally, or by any more sophisticated technique. Here we use these constants as variational parameters in variational Monte Carlo (VMC) calculations, where the local constraint is enforced exactly and the values of the optimal parameters determine the (U(1), Z_2 , or other) nature of the ground state. We defer the results of this analysis to the following subsection.

C. Variational Monte Carlo

The essential physics of the VMC approach is that the local constraint is enforced by Gutzwiller projection. The variational parameters optimizing the projected state are determined by energy minimization (see main text) using Monte Carlo methods and all physical quantities can be calculated from this optimal state. Thus although VMC is based on the mean-field solution, it is far more advanced than the mean-field level, and as such has been used to gain insight into the physics of strongly interacting electron systems ranging from high-temperature superconductors to fractional quantum Hall liquids. In the context of QSLs, the Gutzwiller-projected state provided by VMC can be used to construct the exact ground state of certain exactly solvable models, including the pure Kitaev model on the honeycomb lattice [1] and the Affleck-Kennedy-Lieb-Tasaki model on the spin-1 chain [37]. Because the classification theory of many QSL states is based on slave-parton mean-field methods, VMC can provide the key information as to how the elementary excitations are fractionalized in these cases.

1. Variational Hamiltonian

We comment that there are two approaches to analyzing the competitiveness of a magnetically ordered state. One is to include a magnetic decoupling channel in the spin Hamiltonian, as shown in Eq. (S5). The other is to include an effective external field that induces the magnetic order, as we do on P3 of the main text to obtain the Hamiltonian H'_{mf} . Because the amplitude, $|\mathbf{M}|$, of the (zigzag) ordered component is a variational parameter, these two approaches are entirely equivalent in VMC calculations. In the present study, we have followed the second approach because our aim is to analyze a model reproducing the physics observed in experiment, without dwelling on the complexities encountered by other authors who have studied variations of the same problem

(which we discuss in Sec. S1D).

2. Variational wave functions

In the course of our variational analysis, we have tested the trial wavefunctions of U(1) QSL, Z_2 QSL, Kitaev-type spin-liquid (KSL, a Z_2 QSL state whose dispersion has two Majorana cones in the first Brillouin zone), and partially polarized zigzag-ordered states. The mean-field decoupling of the KSL may be found in Ref. [46]. These studies ascertained that the optimal state we obtain is as close as possible to the true ground state. For the parameter regime of our study (Sec. S1D), which is that inspired by experiment, we find that the competition is always between zigzag order and U(1) QSL (of Dirac or chiral types) states.

Regarding the competitiveness of the Z_2 wave functions at intermediate fields, we resume our discussion of spinon pairing terms within the VMC framework. When particle number is conserved in the mean-field Hamiltonian (i.e. without spinon pairing), the projected state takes the form

$$|\psi_G(\mathbf{p})\rangle_{U(1)} = P_G |\psi_{\text{mf}}(\mathbf{p})\rangle = C_0 \sum_{\alpha} \det A(\mathbf{p}, \alpha) |\alpha\rangle, \quad (\text{S6})$$

where $|\psi_{\text{mf}}(\mathbf{p})\rangle$ is the mean-field ground state with variational parameters \mathbf{p} , $|\alpha\rangle$ is the Ising basis, and C_0 is a normalization constant. $A(\mathbf{p}, \alpha)$ is an $N \times N$ matrix with components $A_{jk}(\mathbf{p}, \alpha) = \langle 0 | c_{j,\alpha_j} \psi_k^\dagger | 0 \rangle$, where c_{j,α_j}^\dagger (Sec. S1A) is the spinon creation operator at site j , with spin component α_j , ψ_k is the k th eigenmode of the mean-field Hamiltonian, which is occupied in the mean-field ground state, and $|0\rangle$ specifies the vacuum state. By contrast, in the presence of spinon-pairing terms, the ground state of the mean-field Hamiltonian is a BCS-type wave function, $|\psi_{\text{BCS}}(\mathbf{p})\rangle = \prod_{i,j,\sigma\sigma'} [1 + a_{i\sigma,j\sigma'}(\mathbf{p}) c_{i,\sigma}^\dagger c_{j,\sigma'}^\dagger] |0\rangle$, where $a_{i\sigma,j\sigma'}$ is the wave function of two spinons in a Cooper pair. After Gutzwiller projection, the Z_2 spin-liquid state takes the form

$$|\psi_G(\mathbf{p})\rangle_{Z_2} = P_G |\psi_{\text{BCS}}(\mathbf{p})\rangle = C_0 \sum_{\alpha} \text{Pf} B(\mathbf{p}, \alpha) |\alpha\rangle, \quad (\text{S7})$$

where $B(\mathbf{p}, \alpha)$ is an $N \times N$ skew-symmetric matrix with components $B_{ij}(\mathbf{p}, \alpha) = a_{i\alpha_i, j\alpha_j}(\mathbf{p})$.

Energy	$\mathbf{B} = 0.2[1, -1, 0]$	$\mathbf{B} = 0.4[1, -1, 0]$	$\mathbf{B} = 0.5[1, -1, 0]$
E_{KSL}	-0.6383	-0.7391	-0.7952
E	-0.6549	-0.7455	-0.7990
E_0	-0.6550	-0.7456	-0.7991

TABLE S1. Ground-state energies obtained from VMC calculations with different applied magnetic fields (taken for this comparison to have the same orientation). E_{KSL} is the energy of the optimized KSL state. E denotes the energy obtained by allowing the variational parameters $\Delta_{0,1,2}^\gamma$ to change freely, E_0 the energy obtained by setting $\Delta_{0,1,2}^\gamma$ to zero. Fields and energies are quoted in units of $|K|$.

We consider applied fields with different orientations and with a magnitude above the first critical field (main text), such that the low-field magnetic order is completely suppressed. The optimal wave functions given by our VMC calculations are such that all three spinon-pairing parameters are always very small, with $\Delta_{0,1,2}^\gamma/t_1^\gamma \approx 10^{-2}$. Because of the BCS-type nature of the wave function of a Z_2 spin liquid [Eq. (S7)], the pairing parameters, $\Delta_{0,1,2}^\gamma$, are never identically equal to zero in the variational process. Thus we repeat the calculation by fixing $\Delta_{0,1,2}^\gamma$ to zero. The results, displayed in Table S1, show clearly that the energy is unchanged or falls even lower, meaning that the U(1) spin liquid is favored energetically. For this reason we have neglected the spinon-pairing terms [second line of Eq. (S5)] in all of our considerations in the main text.

In Table S1 we show also the energy of the optimal KSL state, which we find to be quite uncompetitive except at small values of $\Gamma/|K|$. The apparent convergence of KSL and U(1) energies with increasing field is due largely to spin polarization rather than to competition and is cut off by the phase transition to the trivial paramagnet (occurring, from Fig. 4(a) of the main text, at $B_c/g\mu_B|K|$). Because the mean-field decoupling of the KSL [46] proceeds differently from Eq. (S5), this state cannot reduce to a U(1) state by the vanishing of off-diagonal expectation values.

3. Benchmarking VMC by ED

All of the VMC calculations we use to establish the magnetic order parameter and phase diagram for different field directions (Figs. 3 and 4 of the main text), and the corresponding spinon dispersions and gaps shown in Sec. S3, are performed on systems of 8×8 2-site unit cells (i.e. 128 sites). We conclude this subsection by commenting on the benchmarking of these calculations, and of the optimal wave functions we construct, by comparison with exact-diagonalization calculations. We consider only our variational wave functions with no spinon pairing. We have performed ED on clusters of 2×2 , 2×4 , and 3×3 unit cells, meaning systems with 8, 16, and 18 sites. For these system sizes, variational calculations can be performed in full without resort to MC methods; because the efficacy of MC sampling methods is not in question, the comparison therefore serves to benchmark our variational procedure. In addition to the energies of these

cluster size	E_{ED}	E_v	relative error	overlap
8 sites	-0.6763	-0.6651	1.66%	98.84%
16 sites	-0.6476	-0.6181	4.56%	88.22%
18 sites	-0.6533	-0.6223	4.74%	89.44%

TABLE S2. Ground-state energies obtained from ED and variational calculations on three different clusters, relative errors and wave-function overlaps. Energies are quoted in units of $|K|$.

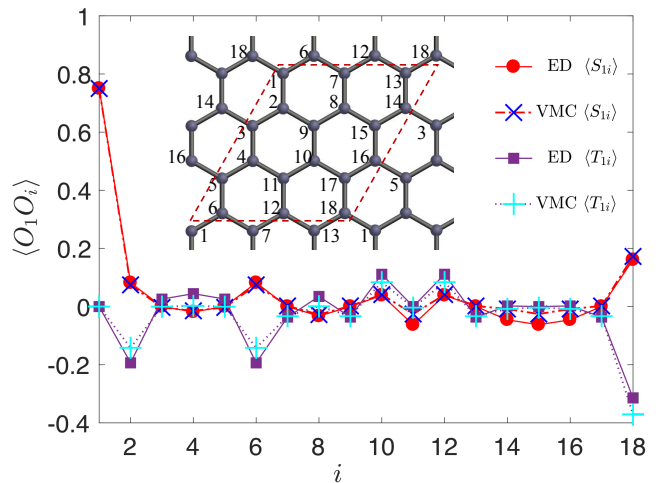


FIG. S1. Spin correlation functions, $S_{1i} = \langle \mathbf{S}_1 \cdot \mathbf{S}_i \rangle$, and off-diagonal symmetric correlation functions, $T_{1i} = \langle S_1^x S_i^y + S_1^y S_i^x + \langle S_1^z S_i^z + S_1^z S_i^y + S_1^y S_i^z \rangle$, between site 1 and all other sites i in the 18-site (3×3 unit-cell) cluster.

systems, we have computed the overlap, $\langle \psi_v | \psi_{ED} \rangle$, of the variational and ED wave functions to test their common content. We have also calculated the conventional and symmetric off-diagonal spin correlation functions, which are observables reflecting the spin state of both systems. As a result of the small ED system sizes, the zigzag magnetization is zero, and thus we cannot benchmark the magnetic order by this method (from VMC we find that system sizes of at least 4×4 unit cells are required for finite $|\mathbf{M}|$). The energies and overlaps shown in Table S2 indicate a very close agreement, at the 90% level for 16- and 18-site systems and the 99% level on the 8-site system. The correlation functions, shown for the 18-site system in Fig. S1, demonstrate that the optimized variational states we have constructed do indeed capture all of the primary properties of the magnetic state of the system.

D. Parameters for modelling α -RuCl₃

It is necessary here to comment on the parameters required to model the physical properties of the α -RuCl₃ system and on our choice of minimal model. The (J, K, Γ, \dots) parameter set appropriate for α -RuCl₃ has been the subject of significant controversy, with not only the magnitudes but the signs and indeed the very presence of the different possible parameters being strongly contested. An excellent compilation, and the most comprehensive discussion to date, are provided in the recent study of Ref. [30].

These authors show 3 scenarios for zigzag magnetic order in the zero-field ground state of the classical K - J - Γ model [30]. Of these, only one is consistent with the highly anisotropic magnetization measured in α -RuCl₃ [13]. This result, which has been interpreted as an ef-

fective c axis g factor of only 0.4, can in fact be taken as evidence for a large and negative K combined with a larger and positive Γ . Noting that the J values invoked are small, our current understanding of the situation is that the magnetization and the signs and magnitudes of K and Γ are important in α -RuCl₃, whereas the zigzag order is the consequence of weak J terms and thus is a relatively minor issue. Different authors have proposed several different combinations of possible J terms to achieve zigzag order [38, 39]. The difficulty in deciding among these is compounded by the problem of extracting the properties of the quantum model from a knowledge of the classical one: as examples, we believe that the multi- Q state obtained in Ref. [30] under the physically reasonable (K, Γ) scenario with a weak ferromagnetic (FM) nearest-neighbor J term, and indeed any incommensurate- Q state, would not be present in a quantum model.

As stated in the main text, a linear spin-wave treatment based on this minimal K - Γ model, with parameters $K < 0$, $\Gamma > 0$, and $\Gamma > |K|$, was found to provide a good fit to the spectrum of gapped (anisotropic) spin waves measured at zero field [29]. Our variational treatment of the zigzag magnetic order within this model was motivated by the result [15] that a zigzag-ordered ground state is favored within the single- Q approximation. Subsequent analysis [30] has shown that the classical model does not in fact support zigzag order without FM Heisenberg interactions. We stress again that rather little is known about the fully quantum K - Γ model.

The observation most important for the present work is the following. To include a FM Heisenberg interaction within the slave-fermion framework, it is most transparent to express this in the form

$$-\mathbf{S}_i \cdot \mathbf{S}_j = -\frac{1}{4}(C_i^\dagger \boldsymbol{\sigma} C_j \cdot C_j^\dagger \boldsymbol{\sigma} C_i + C_i^\dagger \boldsymbol{\sigma} \bar{C}_j \cdot \bar{C}_j^\dagger \boldsymbol{\sigma} C_i), \quad (\text{S8})$$

which is identical to Eq. (S2) up to a different constant. Because the vector parameters $\langle C_i^\dagger \boldsymbol{\sigma} C_j \rangle$ and $\langle C_i^\dagger \boldsymbol{\sigma} \bar{C}_j \rangle$ contain only combinations of the $t_{0,1,2,3}^\gamma$ and $\Delta_{0,1,2,3}^\gamma$ terms which are already present in the Hamiltonian of Eq. (S5), the inclusion of a weak J_1 [30] or J_3 term [38, 39] leads only to a small quantitative rescaling of the parameters of the system and cannot cause qualitative alterations to the nature of the spin-liquid state. We stress that this statement includes the issue of possible spinon-pairing terms discussed in Secs. S1B and S1C: while these may indeed become more favorable for large changes to the input parameters, they cannot appear as a direct consequence of very small J_1 or J_3 terms. Thus all the primary conclusions of our variational analysis are robust against small changes to the model parameters and this is the sense in which we assert that the minimal K - Γ model is fully representative of the extended Kitaev system in the general parameter space relevant to α -RuCl₃.

S2. DIRAC CONES: SIGN OF MASS AND CHERN NUMBER

In this section we present a complete analysis of the combined symmetries of the honeycomb lattice and the spin-orbit-coupled spin sector, which act to protect the Dirac cones in the mean-field dispersion of Eq. (2) of the main text. For simplicity, we consider the case with $t_1 = 1$, $t_0 = t_2 = 0$, and $|\mathbf{B}| = 0$, where the mean-field Hamiltonian becomes

$$H_{\text{mf}} = -i \sum_{\langle i,j \rangle \in (\alpha\beta)\gamma} C_i^\dagger (\sigma_\alpha + \sigma_\beta) C_j. \quad (\text{S9})$$

We expand Eq. (S9) in Fourier space and consider the Dirac cones centered at the different points shown in Fig. 2(b) of the main text.

A. Points K and K'

The wave vector \mathbf{K} is invariant under the action of a C_{3v} group. Because C_{3v} is a symmetry of the mean-field Hamiltonian (S9), the Fourier component $H_{\mathbf{K}}$ must be invariant under the action of C_{3v} . Due to the spin-orbit coupling, the full symmetry is a combination of spin and sublattice operations, for which an explicit expression can be obtained by considering the Hamiltonian component

$$\begin{aligned} H_{\mathbf{K}} &= -i C_{\mathbf{K},A}^\dagger [(\sigma_x + \sigma_y)\omega + (\sigma_y + \sigma_z) \\ &\quad + (\sigma_x + \sigma_z)\omega^2] C_{\mathbf{K},B} + \text{h.c.} \\ &= C_{\mathbf{K}}^\dagger \left[-\mu_y \otimes \sigma_x + \left(\frac{\sqrt{3}}{2} \mu_x + \frac{1}{2} \mu_y \right) \otimes \sigma_y \right. \\ &\quad \left. + \left(-\frac{\sqrt{3}}{2} \mu_x + \frac{1}{2} \mu_y \right) \otimes \sigma_z \right] C_{\mathbf{K}}, \quad (\text{S10}) \end{aligned}$$

in which $\omega = e^{i\frac{2\pi}{3}}$, $C_{\mathbf{K},\alpha}^\dagger = (c_{\mathbf{K},\alpha,\uparrow}^\dagger \ c_{\mathbf{K},\alpha,\downarrow}^\dagger)$, where the index $\alpha = A, B$ represents the two sublattices of the honeycomb system, and $C_{\mathbf{K}}^\dagger = (C_{\mathbf{K},A}^\dagger \ C_{\mathbf{K},B}^\dagger)$. The Pauli-matrix operators μ_m , with $m = x, y, z$, act on the sublattice degrees of freedom while the operators σ_m act on the spin degrees of freedom.

A graphical understanding of the operator content of Eq. (S10) is provided in Fig. S2(a). Each of the three terms in the square brackets is a direct product of two 2×2 matrices, $\mu_n \otimes \sigma_l$, which we express in the form $\mu_{\mathbf{n}} \otimes \sigma_{\mathbf{l}}$, with $\mu_{\mathbf{n}} = \boldsymbol{\mu} \cdot \hat{\mathbf{n}}$ and $\sigma_{\mathbf{l}} = \boldsymbol{\sigma} \cdot \hat{\mathbf{l}}$. $\hat{\mathbf{n}}$ and $\hat{\mathbf{l}}$ are each a set of unit vectors determining the action of the operators, with $\hat{\mathbf{l}}$ being simply the spin basis vectors ($\hat{x}, \hat{y}, \hat{z}$) encountered in Fig. 1(a) of the main text. As shown in Fig. S2(a), the corresponding $\hat{\mathbf{n}}$ vectors form a non-orthogonal set spanning a plane; although the μ_m matrices operate in a somewhat abstract sublattice space, the hopping matrix elements related by μ_x and μ_y are subject to the symmetries of the honeycomb plane, and the μ_z operator is orthogonal to both. Vectors of the same color in Fig. S2(a) are connected by the same term in Eq. (S10). The C_3 rotation operation is a simultaneous

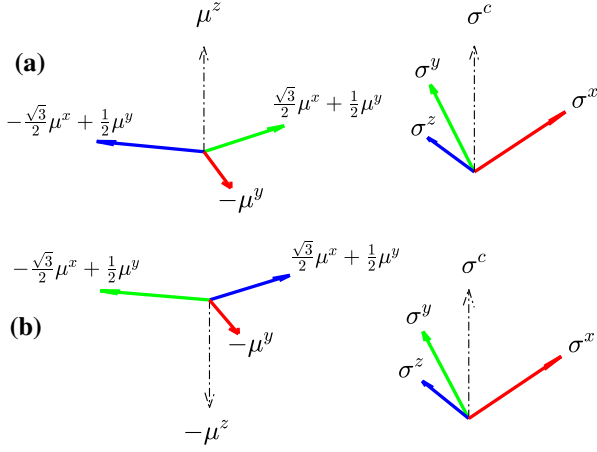


FIG. S2. Schematic representation of the operator content of the combined sublattice and spin symmetries contained in the minimal model of Eq. (S10) for the K point of the Kitaev honeycomb system in the geometry presented by the materials Na_2IrO_3 and $\alpha\text{-RuCl}_3$. The left panels show the three directions in the sublattice space connected by the μ_x and μ_y operations, to which μ_z is orthogonal, while the right panels show the three directions in spin space governing the action of σ_x , σ_y , and σ_z . Vectors of the same color appear in the same terms in the Hamiltonians, $H_{\mathbf{K}}$ in panel (a) and $H_{\mathbf{K}'}$ in panel (b). The dot-dashed lines mark the axis of the C_3 symmetry, which causes a cyclic permutation of both sets of vectors.

cyclic permutation of the three $\hat{\mathbf{n}}$ vectors and the three $\hat{\mathbf{l}}$ vectors, while a mirror operation is a simultaneous exchange of two out of each set of basis vectors. Thus it is clear that the matrix operators representing the generators of the C_{3v} symmetry may be written as

$$C_3 = e^{-i\frac{\mu_z}{2}\frac{2\pi}{3}} \otimes e^{-i\frac{\sigma_z}{2}\frac{2\pi}{3}}, \quad (\text{S11})$$

$$M_z = \left(\frac{1}{2}\mu_x + \frac{\sqrt{3}}{2}\mu_y\right) \otimes \frac{1}{\sqrt{2}}(\sigma_x - \sigma_y), \quad (\text{S12})$$

with $\sigma_c = \frac{1}{\sqrt{3}}(\sigma_x + \sigma_y + \sigma_z)$, which is contained in Eq. (3) of the main text. The C_{3v} symmetry is non-Abelian and protects the twofold energy-level degeneracy at the K point, which gives rise to a Dirac cone.

Because $\mathbf{K}' = -\mathbf{K}$, the Hamiltonian at K' can be obtained by exchanging ω with ω^2 , whence

$$H_{\mathbf{K}'} = C_{\mathbf{K}'}^\dagger \left[-\mu_y \otimes \sigma_x + \left(-\frac{\sqrt{3}}{2}\mu_x + \frac{1}{2}\mu_y\right) \otimes \sigma_y + \left(\frac{\sqrt{3}}{2}\mu_x + \frac{1}{2}\mu_y\right) \otimes \sigma_z \right] C_{\mathbf{K}'}, \quad (\text{S13})$$

and the generators of C_{3v} at K' are represented as

$$C'_3 = e^{i\frac{\mu_z}{2}\frac{2\pi}{3}} \otimes e^{-i\frac{\sigma_z}{2}\frac{2\pi}{3}},$$

$$M'_z = \left(-\frac{1}{2}\mu_x + \frac{\sqrt{3}}{2}\mu_y\right) \otimes \frac{1}{\sqrt{2}}(\sigma_x - \sigma_y),$$

which is represented in Fig. S2(b) and constitutes the other half of Eq. (3) of the main text.

Next we note that the mean-field Hamiltonian (S9) has spatial-inversion symmetry, $C_i = \{E, P\}$, which is

a subgroup of the full symmetry group, D_{3d} . The inversion operation reverses the sign of the wave vector, i.e. $\hat{P}\mathbf{k} = -\mathbf{k}$. When acting on the matrix elements of the Hamiltonian, this is equivalent to reversing the bond direction, which is the same as permuting the sublattice indices. This result can be observed by considering the relation between $H_{\mathbf{K}'}$ and $H_{\mathbf{K}}$, which yields

$$\hat{P}H_{\mathbf{K}}\hat{P}^{-1} = H_{\mathbf{K}'} = C_{\mathbf{K}'}^\dagger \mathcal{H}_{\mathbf{K}'} C_{\mathbf{K}'} = C_{\mathbf{K}', \mu_y}^\dagger \mathcal{H}_{\mathbf{K}} \mu_y C_{\mathbf{K}'},$$

where $\mathcal{H}_{\mathbf{K}}$ denotes the matrix Hamiltonian operator within $H_{\mathbf{K}}$ and $\mu_y \equiv \mu_y \otimes I$ denotes the combined operator with sublattice and spin components. Thus for any general momentum, \mathbf{k} , the relation $\hat{P}H_{\mathbf{k}}\hat{P}^{-1} = H_{-\mathbf{k}}$ means that $H_{\mathbf{k}}$ has the property

$$\mathcal{H}_{-\mathbf{k}} = \mu_y \mathcal{H}_{\mathbf{k}} \mu_y. \quad (\text{S14})$$

Further, because the Hamiltonian contains no intra-sublattice (second-neighbor) spinon hopping terms, and thus contains only μ_x and μ_y , spatial inversion can be used to deduce the additional property

$$\mu_z \mathcal{H}_{\mathbf{k}} \mu_z = -\mathcal{H}_{\mathbf{k}}. \quad (\text{S15})$$

From these symmetries of the Hamiltonian, it is possible to read out two important pieces of information, namely (i) which types of perturbation will break the total symmetry, causing a gap to open in the Dirac cones, and (ii) if the Dirac cones are gapped, what the resulting Chern number should be.

To obtain this information, we focus on wave vectors near the two Dirac points. When a Dirac cone is gapped, a half-quantized Chern number $\mathcal{C} = \pm\frac{1}{2}$ is obtained [40–42]. The sign of the Chern number is also said to be the sign of the mass. To analyze the total Chern number of the Dirac cones, we define the matrix Hamiltonian operators

$$\delta\mathcal{H}(\delta\mathbf{k}) = \mathcal{H}_{\mathbf{K}+\delta\mathbf{k}} - \mathcal{H}_{\mathbf{K}},$$

$$\delta\mathcal{H}'(\delta\mathbf{k}) = \mathcal{H}_{\mathbf{K}'+\delta\mathbf{k}} - \mathcal{H}_{\mathbf{K}'},$$

and keep only those terms linear in $\delta\mathbf{k}$ at small $|\delta\mathbf{k}|$. This approximation is in general reliable because the primary contributions to the Chern number in the presence of a mass term are from states very close to the Dirac point. By substituting Eq. (S15) into (S14), we deduce that $\mathcal{H}_{-\mathbf{k}} = -\mu_x \mathcal{H}_{\mathbf{k}} \mu_x$ and hence

$$\begin{aligned} \mu_x \delta\mathcal{H}(\delta\mathbf{k}) \mu_x &= -(\mathcal{H}_{-\mathbf{K}-\delta\mathbf{k}} - \mathcal{H}_{-\mathbf{K}}) \\ &= -(\mathcal{H}_{\mathbf{K}'+\delta\mathbf{k}} - \mathcal{H}_{\mathbf{K}'}) \\ &= -\delta\mathcal{H}'(-\delta\mathbf{k}) = \delta\mathcal{H}'(\delta\mathbf{k}), \end{aligned} \quad (\text{S16})$$

where the last equality follows from the assumption of linearity.

As noted in the main text, there are two types of mass term which break the C_{3v} symmetry and gap the pair of Dirac cones at K and K' , namely a sublattice chemical potential, $\lambda\mu_z$, and a Zeeman field term, $g\mu_B\sigma_c$. Without knowing any details of $\mathcal{H}_{\mathbf{K}+\delta\mathbf{k}}$, it is clear from their differing operator structures that the two mass terms yield different total Chern numbers.

To demonstrate that the sublattice potential term gives a trivial total Chern number, we show that the $\lambda\mu_z$ term has different signs for the mass term at the two Dirac cones. At the K point, the perturbed Hamiltonian giving the dispersion a massive Dirac-cone form is

$$h(\delta\mathbf{k}, \lambda) = \delta\mathcal{H}(\delta\mathbf{k}) + \lambda\mu_z.$$

From Eq. (S16), at the K' point one has

$$\begin{aligned} h'(\delta\mathbf{k}, \lambda) &= \delta\mathcal{H}'(\delta\mathbf{k}) + \lambda\mu_z \\ &= \mu_x \delta[\mathcal{H}(\delta\mathbf{k}) - \lambda\mu_z] \mu_x \\ &= \mu_x h(\delta\mathbf{k}, -\lambda) \mu_x. \end{aligned}$$

Because a global unitary transformation such as μ_x does not change the topological properties of the ground state, the Chern number of $h'(\delta\mathbf{k}, \lambda)$ must equal that of $h(\delta\mathbf{k}, -\lambda)$, which cancels the contribution from $h(\delta\mathbf{k}, \lambda)$, and therefore the total Chern number contributed by the mass term $\lambda\mu_z$ is zero.

To demonstrate that the Zeeman term gives a non-trivial total Chern number, we compare the two gapped Dirac Hamiltonians

$$\begin{aligned} h(\delta\mathbf{k}, B_c) &= \delta\mathcal{H}(\delta\mathbf{k}) + g\mu_B B_c \sigma_c, \\ h'(\delta\mathbf{k}, B_c) &= \delta\mathcal{H}'(\delta\mathbf{k}) + g\mu_B B_c \sigma_c. \end{aligned}$$

Because μ_x commutes with σ_c , from (S16) we have

$$h'(\delta\mathbf{k}, B_c) = \mu_x (\delta\mathcal{H}(\delta\mathbf{k}) + g\mu_B B_c \sigma_c) \mu_x = \mu_x h(\delta\mathbf{k}, B_c) \mu_x.$$

From the fact that $h(\delta\mathbf{k}, B_c)$ and $h'(\delta\mathbf{k}, B_c)$ are related by a global unitary transformation, they must always have the same Chern number, i.e. $+1/2$ or $-1/2$. As a consequence, the total Chern number of the two Dirac cones contributed by the mass term $g\mu_B B_c \sigma_c$ is either 1 or -1 .

B. Points K_x and K'_x

Following the notation and logic of the previous subsection, the K_x component of the Hamiltonian is

$$H_{\mathbf{K}_x} = C_{\mathbf{K}_x}^\dagger [\mu_x \otimes (-\sigma_y + \sigma_z) + \mu_y \otimes (\sigma_y + \sigma_z)] C_{\mathbf{K}_x}.$$

Although the momentum \mathbf{K}_x has a relatively low symmetry, as is evident from Fig. 2(b) of the main text, the Hamiltonian at this point has an emergent non-Abelian C_{4v} symmetry, whose two generators are

$$C_4 = e^{-i\frac{\mu_z}{2}\frac{\pi}{2}} \otimes e^{i\frac{\sigma_x}{2}\frac{\pi}{2}}, \quad (\text{S17})$$

$$M_x = \mu_x \otimes \frac{1}{\sqrt{2}}(\sigma_y - \sigma_z), \quad (\text{S18})$$

as stated in Eq. (4) of the main text. Similar to the treatment of the K and K' points, the Hamiltonian term $H_{\mathbf{K}'_x}$ is related to $H_{\mathbf{K}_x}$ by $\mathcal{H}_{\mathbf{K}'_x} = \mu_y \mathcal{H}_{\mathbf{K}_x} \mu_y$, whence

$$H_{\mathbf{K}'_x} = C_{\mathbf{K}'_x}^\dagger [-\mu_x \otimes (-\sigma_y + \sigma_z) + \mu_y \otimes (\sigma_y + \sigma_z)] C_{\mathbf{K}'_x},$$

and the generators of the emergent C_{4v} symmetry are

$$\begin{aligned} C'_4 &= \mu_y C_4 \mu_y = e^{i\frac{\mu_z}{2}\frac{\pi}{2}} \otimes e^{i\frac{\sigma_x}{2}\frac{\pi}{2}}, \\ M'_x &= \mu_y M_x \mu_y = -\mu_x \otimes \frac{1}{\sqrt{2}}(\sigma_y - \sigma_z). \end{aligned}$$

Following the logic applied at the K and K' points, a mass term $\lambda\mu_z$ gaps the Dirac cones with topologically trivial consequences while a term $g\mu_B B_c \sigma_x$ contributes a nonzero total Chern number of 1 or -1 .

However, the relative signs of the Chern numbers should be treated carefully. From Eq. (S11), μ_z and σ_c define the direction of the C_3 rotation. If either term is added to the Hamiltonian at K , the C_{3v} symmetry is broken in the same way and thus both terms give the same sign of the mass for the resulting Dirac cone. By contrast, Eq. (S17) shows that μ_z and $-\sigma_x$ give the same sign of the mass for the Dirac cones they gap at K_x . Alternatively stated, the Chern number generated by the mass σ_c at the cones K and K' is the same as the Chern number generated by the mass $-\sigma_x$ at the cones K_x and K'_x . Specifically, if $g\mu_B B_c \sigma_c$ term contributes a total Chern number of -1 for the pair of Dirac cones at K and K' , then $g\mu_B B_c \sigma_x$ contributes a net Chern number of 1 for the pair of Dirac cones at K_x and K'_x . The discussion for the other two pairs of cones, K_y, K'_y and K_z, K'_z is the same as the case K_x, K'_x and will not be repeated here. These results underpin the content of Table I in the main text and the expression

$$C = \text{sgn}(\mathbf{B} \cdot \hat{x}) + \text{sgn}(\mathbf{B} \cdot \hat{y}) + \text{sgn}(\mathbf{B} \cdot \hat{z}) - \text{sgn}(\mathbf{B} \cdot \hat{c})$$

deduced there.

The symmetry analysis we have applied at the Dirac points is strictly valid only for the Hamiltonian at $\mathbf{B} = 0$, whereas a finite magnetic field is expected to violate some of its symmetries. However, the conclusions drawn from these symmetry arguments remain valid if the relative field intensity, $g\mu_B |\mathbf{B}|/|K|$, is small. This situation is also analogous to the case of graphene, where the C_{3v} symmetry protects the Dirac cones at K and K' . If a small strain acts to deform the graphene sheet, the C_{3v} symmetry is no longer satisfied rigorously, but the Dirac cones survive with small shifts of their positions in momentum space [43]. In the present analysis, the application of a magnetic field oriented in one of the three directions ($\hat{x} - \hat{y}$), ($\hat{y} - \hat{z}$), or ($\hat{z} - \hat{x}$) results in the Dirac cones at K and K' surviving, but with their positions shifted. In Sec. S3 we demonstrate numerically the robustness of the Dirac cones over a finite range of field intensity, which reflects the fact that they are indeed symmetry-protected.

S3. SPINON DISPERSION RELATIONS

Here we illustrate the form of the spinon dispersion relations obtained when the magnetic field is applied in different directions relative to the crystal axes. We assume that the zigzag magnetic order is suppressed by the action of the field. In general, the spinon band structure

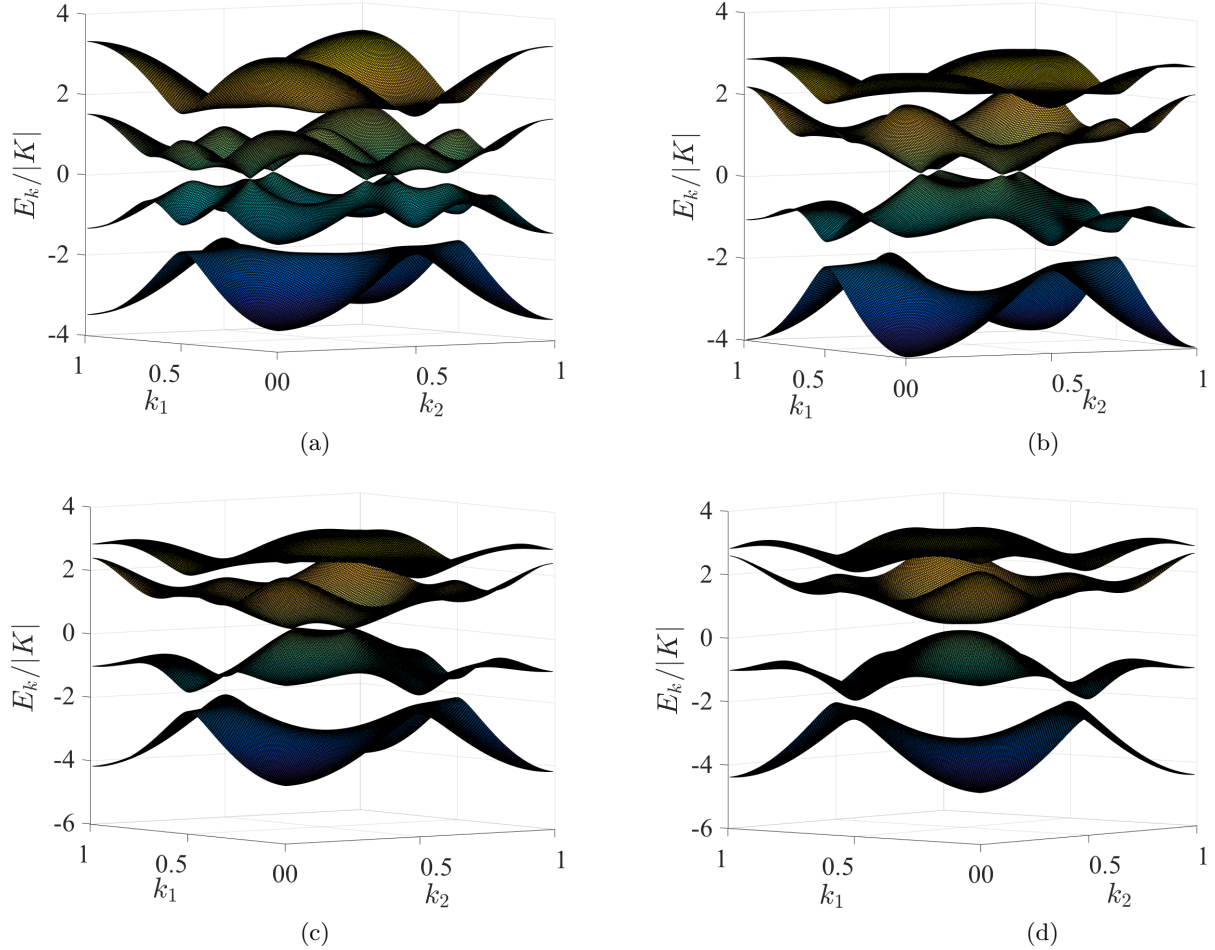


FIG. S3. Spinon dispersion relations of the Dirac spin liquid induced by a magnetic field $\mathbf{B} \parallel \hat{z}$. (a) When $g\mu_B B_z/|K| = 0.16$, there are two pairs of Dirac cones located close to the points K_x, K_y and K'_x, K'_y in Fig. 2(b) of the main text. (b) When the field is increased, the nodes from K_x and K_y , and those from K'_x and K'_y , move toward each other, as illustrated here for $g\mu_B B_z/|K| = 1$. (c) When the field reaches a critical value, $g\mu_B B_z/|K| = 1.25$ in this case, the cones from each pair merge into a single gapless point with semi-Dirac dispersion. (d) When the field is increased further, as shown here for $g\mu_B B_z/|K| = 1.5$, a gap opens and the system enters the trivial gapped phase.

obtained at the mean-field level remains qualitatively unaltered by the Gutzwiller projection, although the band width and band gap are renormalized. The spinon dispersions shown in the figures to follow are computed from the mean-field Hamiltonian with variational parameters adopted from VMC calculations in which the energy of the trial ground state was optimized.

Field-induced Dirac spin liquid. If \mathbf{B} is parallel to one of the directions \hat{x} , \hat{y} , \hat{z} , $(\hat{x} - \hat{y})$, $(\hat{y} - \hat{z})$, or $(\hat{z} - \hat{x})$, there exists a field-induced gapless spin-liquid phase. In Fig. S3 we show the spinon spectrum for the case $\mathbf{B} \parallel \hat{z}$. It is clear that when the field intensity exceeds a lower critical value, required to suppress the zigzag ordered phase (Figs. 3 and 4 of the main text), it induces a spin liquid with two pairs of Dirac cones [Fig. S3(a)]. Increasing the field causes the two cones in the left half of the Brillouin zone to move towards each other, while the pair in the right half behaves symmetrically [Fig. S3(b)]. This

process continues until the cones of each pair merge to form a single gapless point, about which the dispersion is of semi-Dirac type [Fig. S3(c)]. A further increase in field beyond this critical value causes the two new semi-Dirac “cones” to become gapped [Fig. S3(d)].

Field-induced chiral spin liquid. If the field components satisfy the conditions $B_x \neq 0$, $B_y \neq 0$, $B_z \neq 0$, and $B_c \neq 0$ in such a way that $\mathcal{C} \neq 0$, then a chiral spin liquid can be induced. In Fig. S4 we show the spinon dispersion for the case $\mathbf{B} \parallel \hat{c}$, which ensures that $\mathcal{C} = 2$. When the field is sufficiently strong that magnetic order has been suppressed [Fig. S4(a)], which is a first-order transition (Fig. 4(b) of the main text), the resulting gapped phase is a chiral spin liquid. We draw attention to the fact that the gap in question is between the second and third bands (half-filling) in all panels of Fig. S4, whereas the large gap visible between the first and second bands in this case is not relevant. As the field is increased to a critical value,

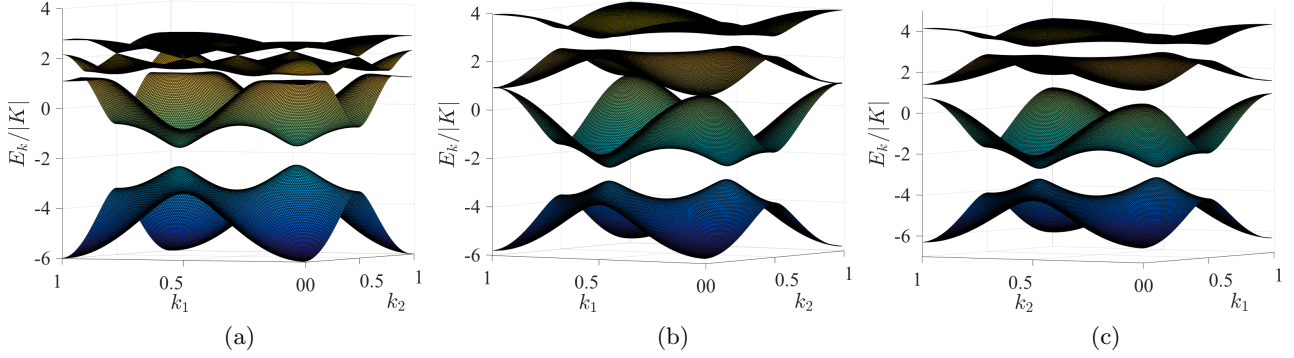


FIG. S4. Spinon dispersion relations of the chiral spin liquid induced by a magnetic field \mathbf{B} applied in the direction $(\hat{x} + \hat{y} + \hat{z})$. (a) When $g\mu_B\mathbf{B}/|K| = (1.4, 1.4, 1.4)$, the spinon band structure is fully gapped and when half-filled has total Chern number $\mathcal{C} = 2$. (b) When the field is increased to a critical value, $g\mu_B\mathbf{B}^c/|K| = (1.8, 1.8, 1.8)$, the gaps close as semi-Dirac “cones” form. (c) When the field is increased further, as shown here for $g\mu_B\mathbf{B}/|K| = (2.2, 2.2, 2.2)$, the gap reopens and the system enters the trivial gapped phase.

the spinon band gap closes at two symmetrical points in the Brillouin zone [Fig. S4(b)]. A further increase in field causes the gap to reopen [Fig. S4(c)] in the topologically trivial gapped phase.

Trivial paramagnetic phase. If field direction is such that the system obeys none of the special symmetries classified in the main text, i.e. $B_x \neq 0$, $B_y \neq 0$, $B_z \neq 0$, and $B_c \neq 0$ with $\mathcal{C} = 0$, then a gapped paramagnetic phase is induced when the field is strong enough to suppress the magnetic order. In this case, there is only one phase transition (Fig. 4(c) of the main text) and the gapped state is connected directly to the fully polarized phase, meaning that it is topologically trivial. In this phase the spinons are confined, making the excitations of the system bosonic.

Also in this phase are the special cases when one of the components B_x , B_y , B_z , or B_c is zero, i.e. for field direc-

tions on the circles shown in Fig. 1(a) of the main text. This situation also has only one phase transition, but, as stated in the main text, the gap of the field-induced paramagnetic phase does not open linearly, following instead an algebraic form. Concerning the size of this gap, in Fig. S5 we show the example $\mathbf{B} \parallel (\hat{x} + \hat{y} - 2\hat{z})$, where the gap scales with the field according to $\Delta \propto |\mathbf{B}|^{2.9}$, making the gap for $g\mu_B|\mathbf{B}|/|K| = 0.24$ only $\Delta \simeq 0.07|K|$. Concerning the algebraic functional form of this gap, we have conducted careful numerical studies to investigate its scaling with the intensity of the applied field (in this analysis we set $M = 0$ and consider very low fields). Figure S6 illustrates two different cases: if $\mathbf{B} \parallel (\hat{x} + \hat{y} - 2\hat{z})$, then the gap scales with the field according to $\Delta \propto |\mathbf{B}|^{2.9}$; if $\mathbf{B} \parallel (\hat{x} + 2\hat{y} - 3\hat{z})$, then $\Delta \propto |\mathbf{B}|^{2.1}$. By contrast, when all of the masses (B_x, B_y, B_z, B_c) are nonzero, regardless

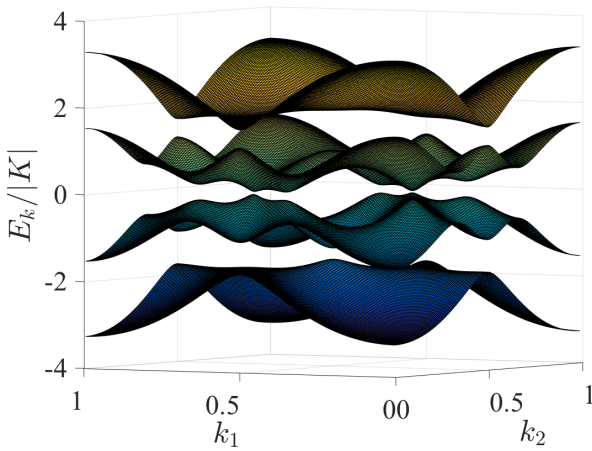


FIG. S5. Spinon dispersion for $g\mu_B\mathbf{B}/|K| = (0.1, 0.1, -0.2)$. Despite this being the trivially gapped paramagnetic phase, the gap remains anomalously small.

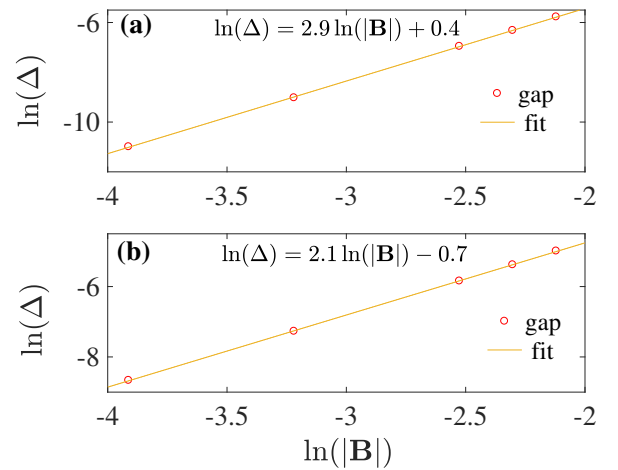


FIG. S6. Scaling of the energy gap, Δ , in the spinon dispersion, shown as a function of the field strength, $|\mathbf{B}|$, on logarithmic axes for two field orientations with $B_c = 0$. (a) $\mathbf{B} \parallel (\hat{x} + \hat{y} - 2\hat{z})$. (b) $\mathbf{B} \parallel (\hat{x} + 2\hat{y} - 3\hat{z})$.

of whether or not the total Chern number is zero, then the gap scales linearly with $|\mathbf{B}|$.

S4. FIELD ORIENTATION AND QUANTUM PHASE TRANSITIONS

It is illustrative to consider the stability of the different spin-liquid states as a function not only of the field strength but also of the angle at which the field is applied. For the special points at which the system has a gapless, four-cone dispersion, this Dirac QSL is not stable: for appropriate field strengths, any change of field angle will cause the system to open a gap. In this sense the $U(1)$ Dirac QSL is different from the Z_2 Kitaev QSL, which is

protected against such small angle changes by the finite vison gap. Along the lines where a change of field angle causes the Chern number to change from $\mathcal{C} = \pm 2$ to 0, the spinon gap closes and the dispersion has two Dirac cones; as discussed in the main text, these are quantum phase transitions between states of confined and deconfined spinons. Because of the finite field strength, these transition lines do not lie strictly on the large circles of Fig. 1 of the main text, but are instead deformed slightly towards the chiral QSL phase, whose regime of stability is therefore a little smaller than Fig. 1 would indicate. The Dirac QSL (four-cone dispersion) points actually mark the meeting of four phases, two with $\mathcal{C} = 0$ and one each with $\mathcal{C} = \pm 2$, and their positions as transition points remain unchanged for any field strength.